Optics and Laser Technology 133 (2021) 106523

Contents lists available at ScienceDirect

Optics and Laser Technology

journal homepage: www.elsevier.com/locate/optlastec

Full length article

Rayleigh scattering characterization of a low-loss MgO-based nanoparticle-doped optical fiber for distributed sensing

Daniele Tosi[a,b,*], Carlo Molardi[a], Wilfried Blanc[c]

[a] Nazarbayev University, School of Engineering and Digital Sciences, 010000 Nur-Sultan, Kazakhstan
[b] National Laboratory Astana, Laboratory of Biosensors and Bioinstruments, 010000 Nur-Sultan, Kazakhstan
[c] Université Côte d'Azur, INPHYNI–CNRS UMR 7010, Parc Valrose, 06108 Nice, France

HIGHLIGHTS

- We report the fabrication and characterization of a low-loss high-scattering fiber for distributed sensing.
- The fiber is fabricated having MgO-based nanoparticles in the core.
- The scattering increment of the fiber is 48.9 dB with two-way losses of 14.3 dB/m.
- The impact of the fiber in distributed fiber sensor networks is discussed, through a performance analysis.
- The fiber is suitable for long-wavelength optical backscatter reflectometry.

ARTICLE INFO

Keywords:
Distributed sensors
Rayleigh scattering
Optical backscattering reflectometry (OBR)
Nanoparticle-doped fiber
Optical fiber

ABSTRACT

We present the fabrication and characterization of a low-loss enhanced backscattering fiber, having the core doped with MgO-based nanoparticles (MgO-NP), for distributed sensing application. The fiber has a scattering increment of 48.9 dB and two-way attenuation of 14.3 dB/m; these are the largest Rayleigh scattering increment paired with the lowest losses for this type of fiber. In this work, we provide a thorough characterization of the fiber performances, and their impact on distributed sensing networks, using scattering-level multiplexing where a 2.4 – 4.0 times extension of sensing length can be achieved.

1. Introduction

Distributed sensors are an established optical fiber technology, which allows the interrogation of multiple weak reflections occurring within the propagation of light waves [1]. From a technological standpoint, the importance of distributed sensing units is emerging as they allow resolving physical parameters such as temperature [2–3], strain [4], shape [5–6] as well as biochemical parameters such as surrounding refractive index [7–8] or humidity [9] in real time and with a narrow spatial resolution, below the centimeter scale; the combination of speed and sensing resolution over distance is unmatched by other sensing technologies such as lab-on-chips or wireless sensor networks [10].

Generally, we can identify two main approaches for distributed sensing, depending on how the weak reflections in the fiber are generated. On one side, we have the possibility of inscribing reflectors in the fibers, such as continuous or ultralong fiber Bragg gratings [11–13], which yield a continuous amount of reflection. The second approach, relies on the scattering properties of the fiber, which provide an extremely weak yet detectable reflection signal at each point of the span. Systems have been designed using both elastic Rayleigh scattering, which is used in optical backscatter reflectometry (OBR) [3], as well as Raman scattering for temperature sensing [14] and Brillouin scattering for acoustic sensing [15].

Rayleigh scattering is one of the primary loss factors of an optical fiber, hence limiting the performance and span lengths of telecommunication systems [16]; as such, research has focused for many years on engineering fibers to reduce their losses down to their theoretical minimum. Since the fibers used in distributed sensing are standard single-mode telecom fibers (SMF), the sensing units have been engineered with photodetectors capable of detecting and resolving extremely low power levels (around the fW level).

However, thanks to the advent of OBR and other distributed sensing units capable of detecting elastic scattering, we are observing a renovated interpretation of the scattering in fibers. Since the Rayleigh scattering is, simply, the amount of power at the detector at each

* Corresponding author at: Nazarbayev University, School of Engineering and Digital Sciences, 010000 Nur-Sultan, Kazakhstan.
E-mail address: daniele.tosi@nu.edu.kz (D. Tosi).

https://doi.org/10.1016/j.optlastec.2020.106523
Received 30 April 2020; Received in revised form 6 July 2020; Accepted 1 August 2020
Available online 17 August 2020
0030-3992/

distance, fibers with enhanced backscattering, i.e. a higher scattering content than a SMF, allow a better signal-to-noise ratio [5–6], and ultimately allow the formation of complex and multi-dimensional sensing networks. The most recent and significant technique has been labeled as scattering-level multiplexing (SLMux) [17–18], in which the scattering level of the fiber is modulated in intensity and length to interrogate multiple channels in a simultaneous scan; this method has been used in multidimensional (2D and 3D [18]) temperature sensing and in 3D shape sensing [19], where a plurality of fibers have been mounted on a minimally invasive medical device. SLMux is an approach that finds its main focus in medical applications.

The techniques proposed by Westbrook *et al.* [20], Yan *et al.* [3], and Monet *et al.* [13] increase the backreflection of the fiber through weak distributed gratings; Loranger *et al.* [21] proposed instead a method based on UV exposure of the fiber. Albeit low-loss, these methods have a very slow fabrication (in the order of hundreds of micrometers per second) and require stripping the fiber jacket, reducing its tensile strength that is needed for medical devices. The most elegant solution has been proposed by Beisenova *et al.* [17–19], using MgO-based nanoparticles-doped fibers (MgO-NP) [22–23]. The fabrication of these fibers is performed by a standard drawing tower, hence at the same speed and with the same preform of SMF fibers; they also can be stripped, cleaved, and spliced to SMF fibers using the same telecom splicers, as their sizes and fusion properties match the SMF (ITU-T Recommendation G.652). The scattering amount is incremented well over a thousand times (37–46 dB), but the high fiber losses (30–292 dB/m) limit the sensing lengths.

In this work, we present and characterize a MgO-NP fiber optimized for long-range SLMux sensing. The fiber has scattering gain (i.e. the increment of scattering over a standard SMF) of 48.9 dB and average losses of 14.3 dB/m (two-way), which are the highest gain and lowest losses recorded so far for MgO-NP fibers. Using the OBR, we perform a complete characterization of the fiber properties, including attenuation spectra, loss uniformity, polarization-dependent losses, strain- and temperature-dependent losses; then, we discuss the impact of the fiber characteristics on SLMux performance.

2. Experimental setup

The MgO-NP fiber has been fabricated with a process similar to [22–23]. The preform was fabricated by conventional MCVD (Modified Chemical Vapor Deposition) process, except the solution doping step which was modified. A Ge-doped silica porous layer of the core was immersed in 3x5 mL of the doping solution (0.1 mol/l of $MgCl_2$ and 1.10^{-4} mol/l of $ErCl_3$ dissolved in ethanol) injected in the horizontally rotating tube and then dried at 1000 °C under an oxygen gas flow (2000 cc). The porous layer was densified at 1800 °C. The tube was collapsed into the preform by heating above 2200 °C. The diameter of the preform was around 10 mm with a 1 mm core diameter. The optical fiber was drawn on a drawing tower by heating the preform at approximately 2000 °C. The fiber sizes are 250/125/10 μm (jacket/cladding/core diameter).

The working principle and experimental setup of the work is sketched in Fig. 1. The interrogator used for the analysis is a commercial OBR based swept-laser interferometer (Luna OBR4600, Luna Inc., Roanoke, US). A span of MgO-NP of length 2.81 has been connected to a standard single-mode fiber (SMF) of length 3.7 m. The MgO-NP has been spliced to the SMF through a standard telecom fiber (Fujikura 12S, SMF-SMF recipe). The OBR laser has been operated on the 1525.0 – 1610.5 nm range, with 10 μm spatial resolution, 3 Hz speed, and no electrical amplification. Time-domain measurements have been performed with a decimation factor of 32 (0.32 mm gauge length); frequency-domain measurements have been performed with 0.2 m integration width, 515 MHz spectral resolution.

Measurements have been acquired on a single channel, in order to eliminate any interference from the analysis, as shown in Fig. 1(a–c). The fiber is intended for use in a SLMux system as shown in Fig. 1(d), using the scattering diversity principle.

3. Results

3.1. Scattering parameters

The scattering trace of the MgO-NP fiber, reporting the power backreflected to the OBR, is shown in Fig. 2. The trace, in dB units, has the typical sawtooth shape observed in SLMux systems [17–19]. The MgO-NP fiber under analysis is a 2.81 m span, beginning at the location 3.71 m; the SMF to MgO-NP splice is almost lossless (loss $<$ 0.1 dB), hence we can observe the difference between the power backscattered by a SMF (-100.9 dBm) and the lead-in portion of the MgO-NP (-52.0 dBm). We define the scattering gain as the increment of scattering between a SMF and the MgO-NP, which is equal to 48.9 dB. The fiber attenuation adheres to an overall linear profile; the average attenuation has been estimated with a linear regression ($R^2 = 0.9990$) to 14.3 dB/m, accounting for both forward and backward scattering.

3.2. Attenuation uniformity

The random nature of the nanoparticle size and distribution observed on a MgO-NP implies that the attenuation properties of the fiber might vary along the fiber length. By performing a piecewise linear regression, we can estimate the attenuation in each location. The results are shown in Fig. 3. From the first chart, we observe that the attenuation has a fluctuating pattern, well visible in the fact that the trace appears to deviate from the inner mean value. The attenuation appears to rise in the first span, and lower at the end. The statistical analysis of the 135 attenuation samples (2.1 cm each) is shown in Fig. 3(b), with the histogram that reports the probability for each value of attenuation. The probability of attenuations are: 0.7% for 10–11 dB/m; 3.0% for 11–12 dB/m; 16.3% for 12–13 dB/m; 28.9% for 13–14 dB/m; 27.4% for 14–15 dB/m; 17.0% for 15–16 dB/m; 5.9% for 16–17 dB/m; 0.7% for 17–18 dB/m. A Gaussian fit of the histogram shows mean value of 14.0 dB/m, with standard deviation of 1.32 dB/m.

3.3. Attenuation spectra

Attenuation spectra have been measured on the OBR by acquiring the Rayleigh scattering signatures at multiple locations around the fiber. The comparison between the amplitude of the return loss at the start and at the end of the MgO-NP span allows estimating the loss spectrum of whole fiber. The result is shown in Fig. 4, in which the measured data have also been filtered with a low-pass digital filter (Butterworth 5th order, cut-off 0.005) to remove the noisy pattern intrinsic in the fiber signatures. We observe that the attenuation has a large variation in the 1525–1610 nm range of the OBR: the attenuation peak is 23.5 dB/m at 1533.3 nm, and it rapidly decreases outside of this range to 16 dB/m at 1527 nm. The rightmost part of the spectrum is the most important part, as we record the lowest losses; here we can apply a 2nd order polynomial fit, which describes the attenuation in the 1541.4 – 1610 nm in an almost perfect way. The attenuation reaches a plateau at 1590–1610 nm, with minimum value of 10.8 dB/m.

In Fig. 5, we report the evaluation of the local attenuation, in order to evaluate the variability of the fiber losses at each location. Fig. 5(a) shows the return loss at each location, which confirms the trend in Fig. 4 with the return loss dip around 1533 nm. By calculating the differential between each location and the next one, and normalizing by each distance, we can evaluate a set of local attenuation data, each spaced by approximately 30–40 cm. The measurement is very noisy, due to the intrinsic noise affecting the backreflection pattern [4,24]; we can observe however some qualitative trend. All data have an attenuation peak around 1533 nm, with different amplitudes, which is in line with the fluctuating trend of the attenuation. The second order

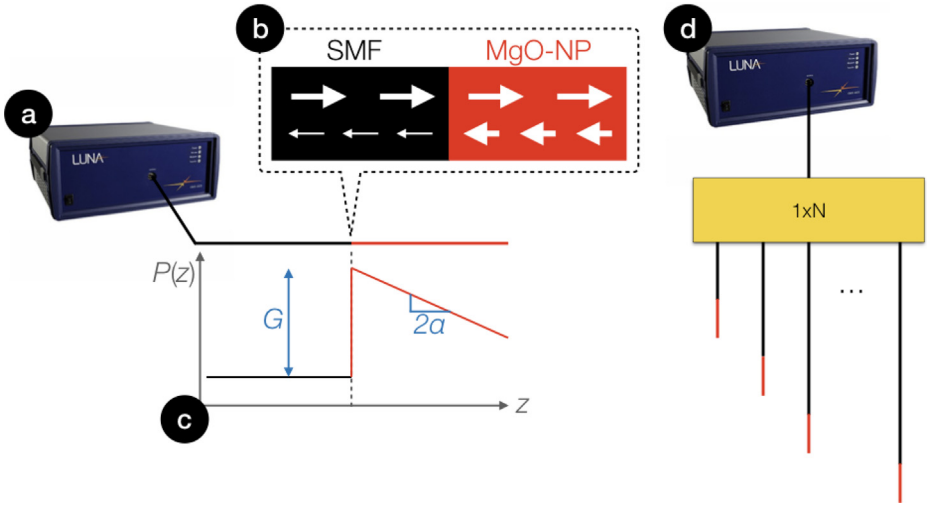

Fig. 1. Sketch of the experimental setup and concept of the work. (a) Schematic of the setup, with an OBR interrogator connected to the MgO-NP fiber through a SMF span. (b) Working principle of the enhanced backscattering fiber, having local reflectivity significantly higher than a SMF. (c) View of the power P backreflected at each location z in logarithmic units, with estimation of scattering gain G and two-way losses 2α. (d) Typical scattering-level multiplexing setup, with a N-channel system; each channel is separated with a 1xN splitter and a network of SMF fibers with different lengths.

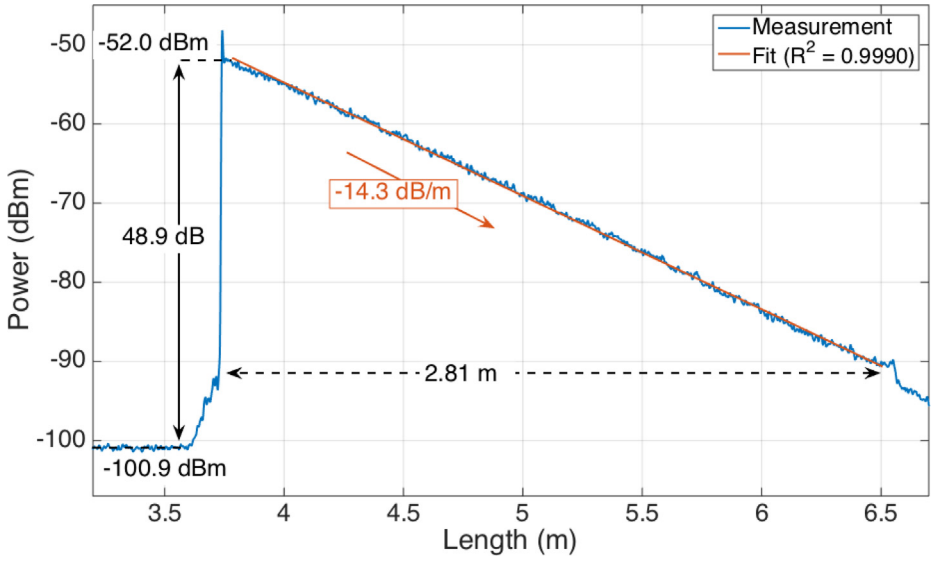

Fig. 2. Backscattering trace of the MgO-NP fiber, reporting the power reflected to the OBR for each location.

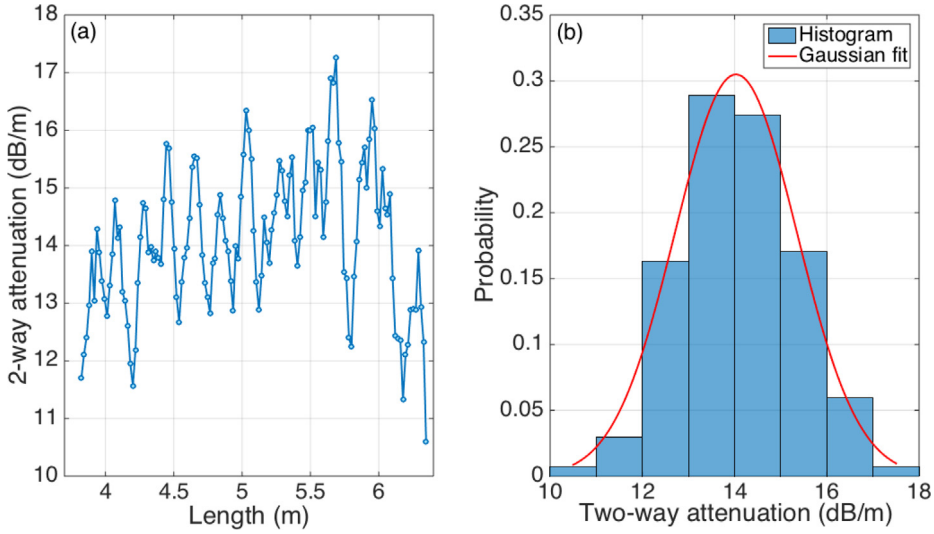

Fig. 3. (a) Estimated fiber attenuation at every location of the MgO-NP fiber, by means of piecewise linear regression; (b) statistical analysis of the attenuation, reporting the probability that the attenuation falls within each value, and its Gaussian fit (R^2 = 0.9925).

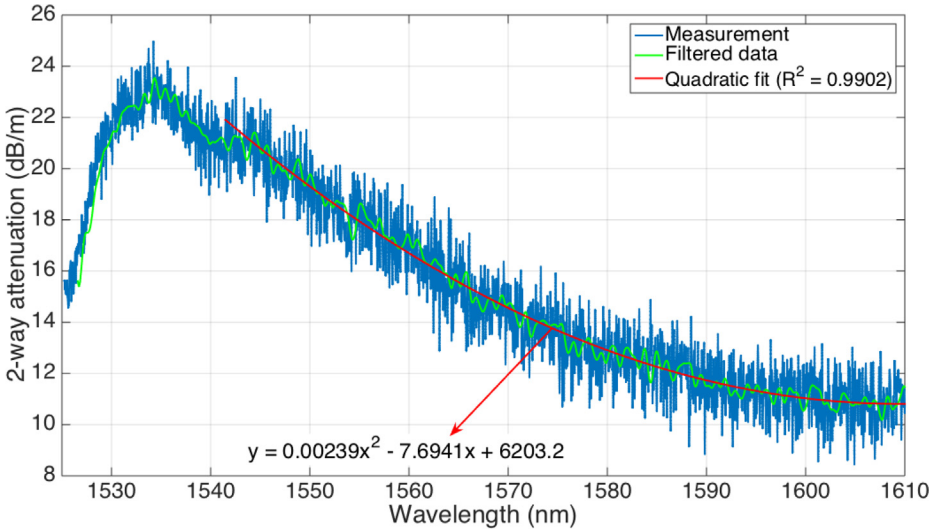

Fig. 4. Attenuation spectrum of the MgO-NP, on the 1525–1610 nm wavelength range. The chart compares the measured data, digitally filtered data to compensate for the noisy pattern, and a second order polynomial fit on the 1541.4 – 1610 nm range.

polynomial fit can also be applied to this measurement, and well describes the attenuation pattern; here we see that all curves appear to have a plateau around 9.0–12.0 dB/m, while the attenuation at 1541 nm is 17.3 – 25.2 dB/m, with a variability within 3 and 8 dB depending on the wavelength.

3.4. Polarization-dependent attenuation

As shown in [3 25], the MgO-NP fiber as well as other scattering-enhancement methods appear to have a polarization-dependent pattern. Using the OBR, we can analyze independently the polarization components, dividing between P (parallel) and S (perpendicular) to the input light source. The measurement has been performed by comparing the attenuation spectra at the input and output side of the MgO-NP fiber, in two points separated by 2.4 m, having the same backscatter level of P and S signals. The results are shown in Fig. 6. We observe that the difference in behavior of the 2 polarizations is not negligible; the S polarization appears to have a lower attenuation at the peak (0.5 dB difference at 1533 nm); however, the losses at the longer wavelengths are higher, 0.7 dB higher than the polarization P, reversing the trend. The differential between P and S is maximum at 1542 nm, equal to 2.2 dB.

3.5. Temperature- and strain-dependent attenuation

In order to evaluate the dependency of the MgO-NP fiber attenuation on the physical parameters (temperature and strain) detected in the sensing network, two separate calibrations have been performed. In the first one, a spool of 2 m of fiber has been immersed in a water bath, which has been heated (33–95 °C) with a hot-plate to measure attenuation spectra at the start and at the end of the heated fiber. In the second experiment, about 1.5 m of fiber have been locked into two micropositioners, applying a calibrated strain (0–900 με); in a similar, fashion, the fiber attenuation has been calculated through the differential of the return loss at the input and output of the strained portions of the fiber.

The results are shown in Fig. 7 for both temperature and strain. The effect of temperature on attenuation is visible; within the 33–95 °C range, which is common in temperature sensing [16], the attenuation follows an almost linear rule with an increase of 4.44×10^{-3} dB/m pear each °C increase, which corresponds to a 1.9% attenuation change (0.3 dB/m) for a range of 57 °C. The strain effects are more negligible: the difference between the maximum and minimum value of attenuation is 0.06 dB/m, and the linear fit shows a coefficient of 5.36×10^{-5} dB/m pear each incremental με.

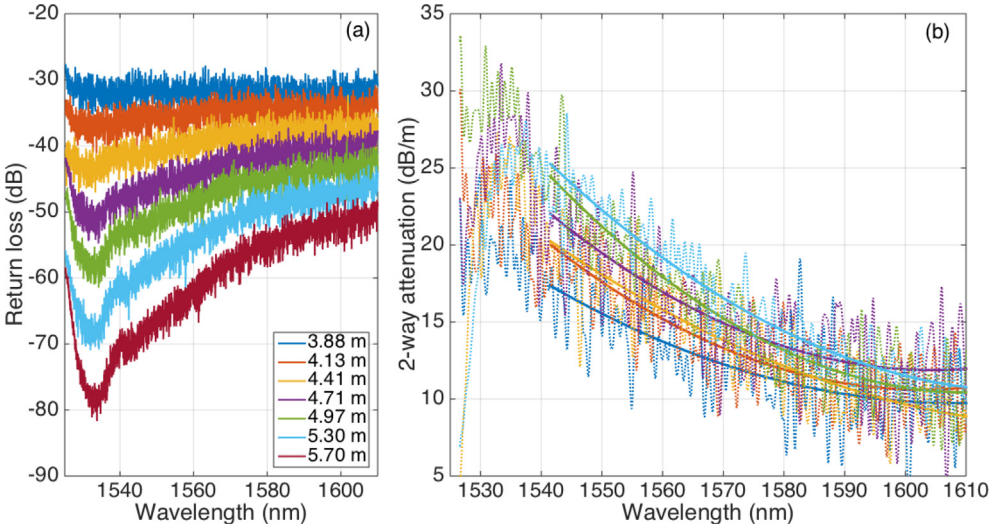

Fig. 5. Local variation of attenuation spectra, and evaluation of the local attenuation of the MgO-NP fiber. (a) Return loss measured at 7 different locations within 3.88 and 5.70 m. (b) Evaluation of the fiber losses for each location, from the differential of return loss values; dotted lines = attenuation data; solid lines = 2nd order fit on 1541.4 – 1610 nm range.

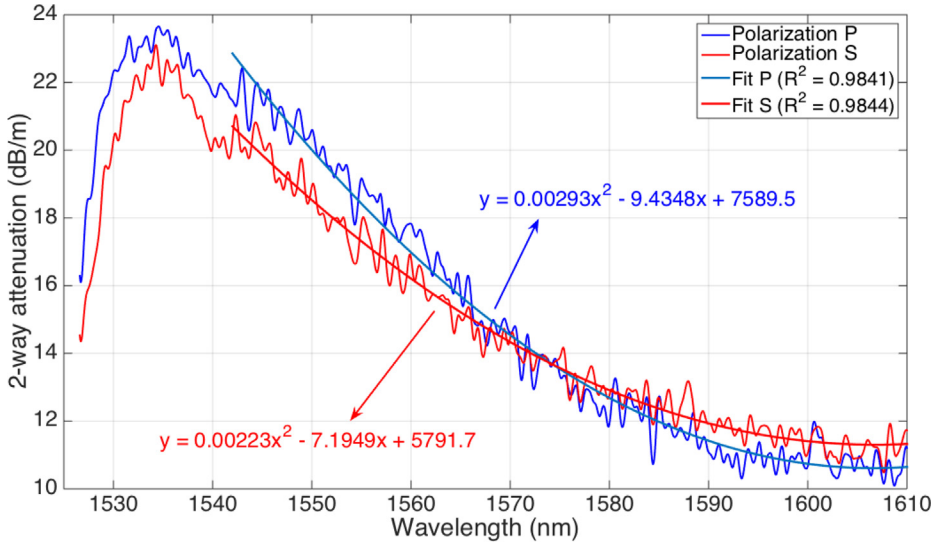

Fig. 6. Evaluation of the polarization-dependent attenuation for the MgO-NP fibers. The attenuation spectra, filtered using the same digital filter as in Fig. 4, are reported for polarizations P and S separately.

3.6. Temperature and wavelength shift sensitivity

A final calibration that is important for sensing is the determination of temperature and strain sensitivity of the fiber, which relate the wavelength shift measured in the return loss spectra at each temperature/strain value. A similar experiment was carried out, using the OBR in distributed sensing mode in one sensing point, to evaluate the wavelength shift values; the results have been obtained by measuring, within the MgO-NP fiber, the correlation peak shift between the measured and reference fiber signatures, i.e. the Rayleigh scattering spectra at the sensing zone.

The results of this calibration are shown in Fig. 8, and are in agreement with [17–18]. The thermal coefficient of the MgO-NP fiber has been estimated as 9.1 pm/°C, while the strain coefficient is 1.0 pm/με. These results are also matching the coefficients of standard silica fibers [4] and Bragg gratings [24] (~10 pm/°C and ~1 pm/με), as expected from the fact that the fiber are based on a silica compound. Hence, the presented MgO-NP fiber demonstrates sensitivity figures similar to SMF and glass fibers, while having the best trade-off between scattering gain and fiber losses presented so far.

4. Discussion

The trade-off between scattering gain (G) and fiber forward and backward attenuation (2α) is at the base of efficient SLMux structures. The fiber presented in this work provides the best performance among MgO-NP fibers and other backscattering enhancing methods. The fiber reported in [8] has G = 32.3 dB and 2α = 27.8 dB/m, while the fiber reported in [17] has G = 36.5 dB and 2α = 25.5 dB/m; the design of these fibers is similar to the one proposed in this work, with MgO nanoparticles distributed along the fiber core. The fiber reported in [26] has G = 46.1 dB and 2α = 292 dB/m, while [7] has G = 47.5 dB and 2α = 298 dB/m. The attenuation figure presented in this work is the lowest between MgO-NP fibers reported so far for SLMux; the fiber has an attenuation that is almost half of the previous MgO-NP fibers reported so far having the inner part of the core doped with the nanoparticles. On the other hand, fibers having a nanoparticle ring have a better scattering gain, and the fiber presented in this work has about 2 dB extra gain over this type of fibers, which however have an attenuation about 50 times higher. Overall, the increment on the gain and attenuation is significant; the scattering of the MgO-NP is 77,600 times

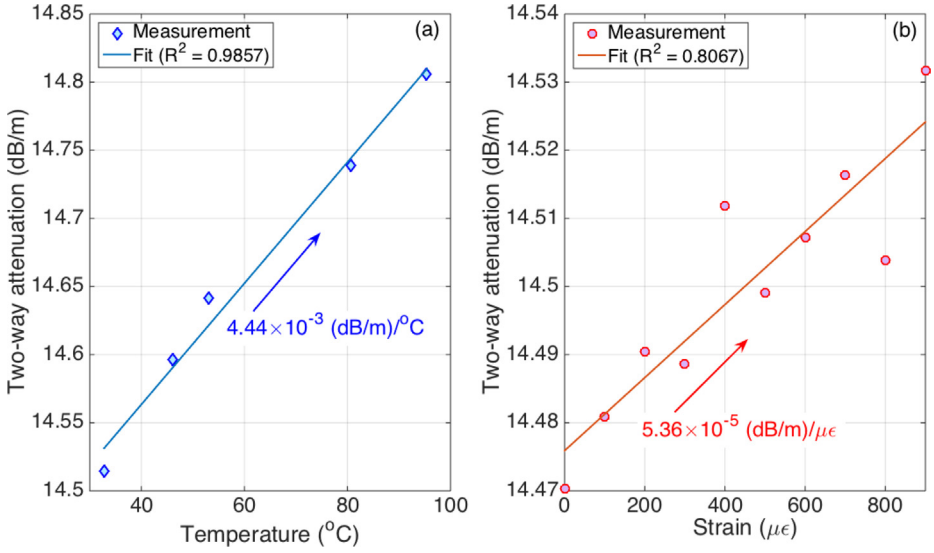

Fig. 7. Evaluation of the temperature and strain effect on fiber attenuation. (a) Temperature-dependent attenuation; (b) Strain-dependent attenuation.

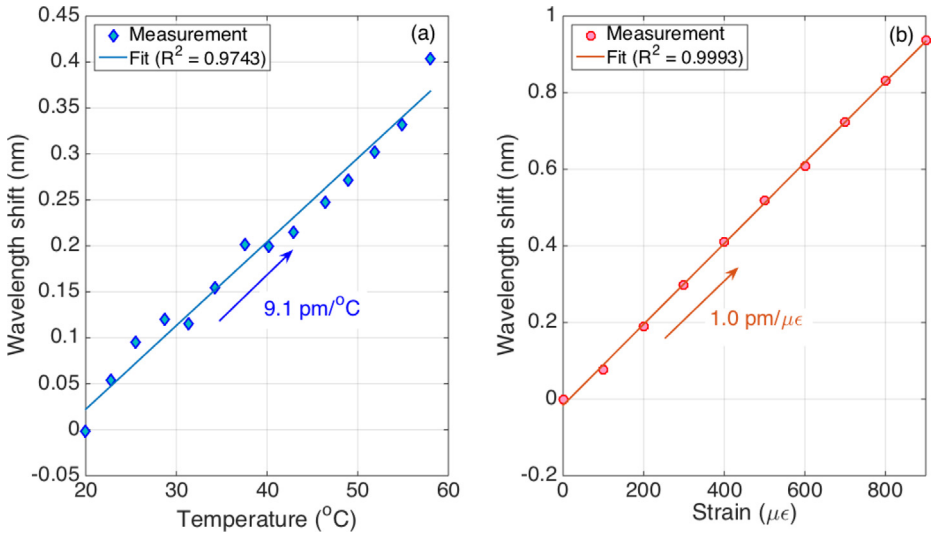

Fig. 8. Wavelength shift of Rayleigh scattering signatures, acquired in frequency domain, as a function of temperature and strain calibration, for the determination of the thermal and strain sensitivity coefficients. (a) Temperature calibration; (b) strain calibration.

more powerful than a SMF fiber. It is to be noted that other enhanced scattering fibers such as the Ge/B doped reported in [6] or the high-Ge doped fiber with high numerical aperture reported in [21] have $G \approx 10$ dB, which makes them unsuitable for SLMux. The methods based on continuous grating inscription have the advantage of having lower losses, but the inscription method is very slow; the most rapid inscription method, reported by Yan *et al.* [3], achieves 1 mm/s direct inscription, with gain around 35 dB an comparable losses (15 dB/m) but it is limited to 15 cm length. Overall, these methods do not have the same easiness of implementation of a standard fiber, but rather require the preparation of each sensing region through a ultraviolet or femtosecond laser. Besides, these methods also require stripping the fiber jacket, a major issue in biomedical devices.

The full characterization of the fiber allows drawing important conclusions and design rules for efficient multi-channel OBR systems. In SLMux or similar arrangement, based on a scattering diversity along N channels as described also in Fig. 1(d) (i.e. one MgO-NP fiber backscatters a certain power at a generic location z, overlapping to N-1 other SMF fibers), we can define the signal-to-interference ratio (SIR), defined as the ratio between the power backscattered by the MgO-NP over the (N-1) SMF fibers interfering with it [17]:

$$SIR(z) = G - 2\alpha z - 10\log_{10}(N-1) \tag{1}$$

where z is the location in the fiber (from the MgO-NP start), N is the number of channels; SIR and G are reported in dB units, 2α in dB/m. By imposing a target SIR, namely SIR_{target}, we can solve for z to obtain the maximum length that we can interrogate, for each channel:

$$L_{max} = \frac{G - 10\log_{10}(N-1) - SIR_{target}}{2\alpha} \tag{2}$$

The Rayleigh scattering losses, as shown in [18–19] and experimentally validated in [17] can be approximated as white Gaussian random processes. Hence, the term 2α refers to the average of the attenuation over the working range of the OBR, considering that as in Fig. 5(a) the return loss spectrum is not at the input side of the MgO-NP.

The other figure that we are going to investigate in conjunction with L_{max} is the spatial resolution Δz. For the OBR, as for any swept-laser method working in frequency domain [1 4], the spatial resolution is:

$$\Delta z = \frac{c}{2n_{eff}\Delta f} \tag{3}$$

where c is the speed of light in vacuum, n_{eff} is the effective refractive index of the fiber (n_{eff} = 1.454 for MgO-NP), and Δf is the sweep frequency range of the laser source.

Now, we can use the characterization of the fiber to understand how to optimize the OBR in terms of L_{max} and Δz and to quantify the impairments. Commercial OBR systems such as the one used in this experiments are based on lasers tunable in the range 1525–1610 nm (equal to 10.61 THz) have a minimum Δz equal to 9.72 μm and work with 2α = 14.3 dB/m. However, we can select a larger spatial resolution, and operate on a portion of fiber where the attenuation is minimum, i.e. at the longest wavelengths. For example, an OBR operating on the 1600–1610 nm would have a 82.6 μm resolution, but would see an attenuation of 11.0 dB/m, which would be 0.5 dB lower if the system operates on a single polarization (P). In most commercial systems the tunable laser can operate on submultiples of the 85-nm range; we consider the cases of 85.0 nm, 42.5 nm, 21.3 nm, 10.6 nm, and 5.3 nm as in the OBR used in this work. The summary of this evaluation is shown in Fig. 9, where we report the value of L_{max} as a function of N for each operative case; we assume the target SIR to be 10 dB, which is a value suitable both for correlation resolving methods [4] and time-domain analysis [26].

The first chart shows the $L_{max}(N)$ function, for each operating condition. As from Eq. (2), the sensing length decreases logarithmically with N. In a full-bandwidth OBR, having the minimum spatial resolution, the maximum length ranges from 1.32 m (N = 64) to 2.46 m (N = 2). Doubling the spatial resolution allows moving away from the 1533 nm attenuation peak, with a resulting increase of sensing length, 1.71 m (N = 64) to 3.20 m (N = 2), i.e. a 21–30% increase. Quadrupling the spatial resolution allows working in proximity of the 1600-nm plateau, with L_{max} approaching 1.9 – 3.6 m. If we can also optimize the polarization, we observe a marginal increase of the performance (2–7 cm additional).

The comparison of the present work with the other MgO-NP fibers is reported in the second chart. Ring-based nanoparticle geometries can be used to interrogate fiber lengths ranging from 7 cm to 13 cm, which is very unpractical for medical applications. The work reported in [8] has the best performance (33 cm to 103 cm). The present work has a significant advantage both in terms of length, and in terms of slope of the $L_{max}(N)$ function. For N = 2 the increment is 2.4 times, but it raises to 4.0 times for N = 64. The possibility of interrogating up to 64 channels, each with length of 2.46 m, means that the implementation of SLMux with the fiber proposed in this work is suitable for multi-functional devices measuring a combination of strain and temperature, for example as in the endoscopes for colonoscopy [27] and gut analysis [28] proposed by Arkwright *et al.* with Bragg grating sensors. Other

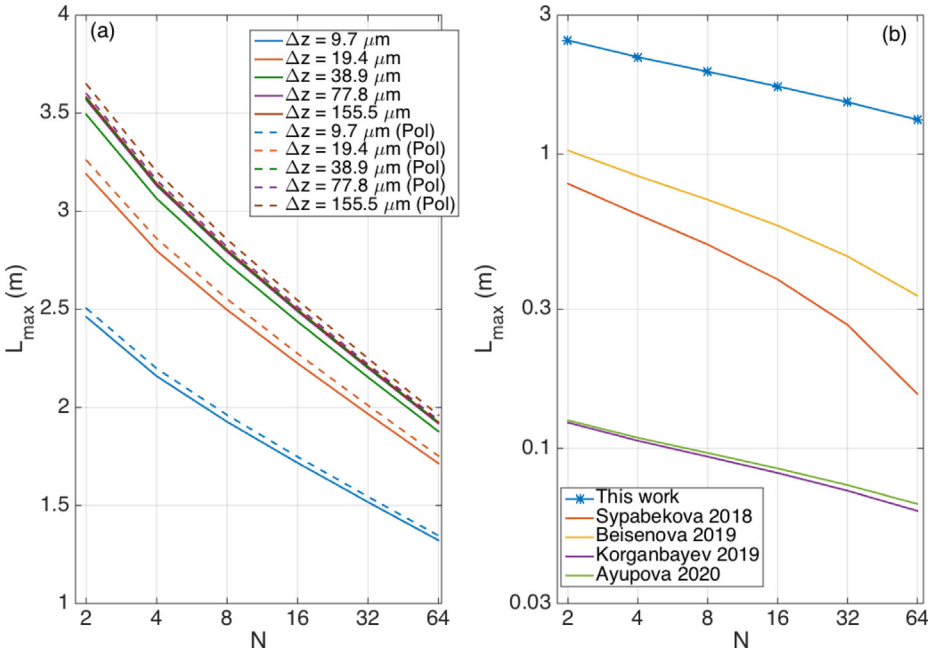

Fig. 9. Performance analysis of OBR, evaluating the $L_{max}(N)$ function for different working conditions. (a) Evaluation of the maximum length as a function of the spatial resolution of the OBR, selecting the wavelength range with the smallest attenuation; the chart reports polarization-insensitive OBR (solid lines), and the polarization-sensitive (Pol) OBR, where the optimal polarization is selected. (b) Comparison of the fiber presented in this work with the other MgO-NP results of Sypabekova [8], Beisenova [18], Korganbayev [26], and Ayupova [7] *et al.* For the present work, the full-bandwidth OBR is shown.

applications for SLMux-based distributed sensing, enabled by a low-loss high-gain MgO-NP fiber, include temperature sensing on 2-dimensional or 3-dimensional grids [18], and shape and strain sensing of medical devices [17,19].

Among the system penalties, the most evident ones are the local variation of the attenuation, which affects the local SIR, and the temperature-dependent losses in high-temperature measurements. The first one is intrinsic in MgO-NP fibers; considering a variation within ± 3 times the standard deviation measured in Fig. 3(b), i.e. (14.0 ± 4.0) dB/m, the attenuation can fluctuate between 10 and 18 dB/m; it corresponds to a 2.16 m – 3.89 m range for L_{max} for $N = 2$, and 1.16 m – 2.09 m range for L_{max} for $N = 64$. This is a large variation, which requires further mitigation for marge networks. The temperature dependency of the attenuation adds another ~2% penalty (or ~1% per each 30 °C of working range) on the L_{max} figure for thermal sensing application. The results obtained in this simulation are in line with the study reported in [29], which finds a logarithmic dependence on the maximum length on the number of channels.

A final consideration can be drawn on the loss mechanism of the MgO-NP and its sensing implications. Fig. 10 shows the attenuation or absorption spectra of the MgO-NP, compared with some notable spectra that include Er-doped fibers with high (Thorlabs Er110-4, 107.5 dB peak absorption) and low (iXblue Er-doped fiber, 9.0 dB peak absorption) doping concentration, absoption spectrum of MgO as in [30], and theoretical Rayleigh scattering according to [16].

As from the chart, the fiber attenuation has a pattern similar to Er-doped fibers, with the peak having a slight shift towards longer wavelengths (about 5 nm difference). Rayleigh scattering plays a role in the attenuation, having a λ^{-4} (λ = wavelength) trend that appears to smooth the decrease of attenuation outside of the Er peak. Overall, the fiber losses appear to have a strong influence on the Er-doping, with a pattern also influenced by the scattering pattern.

Considering that the infrared losses of silica are not a factor in this wavelength range, as they account for about 0.004 dB/m at 1800 nm up to 2.5 dB/m at 2500 nm, this chart shows that it is possible that SLMux system would me more effective at wavelengths longer than 1600 nm, and therefore away from the classical third optical window.

5. Conclusions

In conclusion, we reported the fabrication and characterization of a MgO-NP fiber optimized for distributed sensing. The fiber has 48.9 dB scattering gain and 14.3 dB two-way losses, which are the highest and lowest values reported so far for Rayleigh scattering enhancement. The analysis of the fiber has been reported, reporting attenuation spectra and uniformity, polarization-dependent properties, and thermal and strain effects. The fiber has similar sensitivity to silica fibers to temperature and mechanical strain (9.1 pm/°C and 1.0 pm/με).

A performance analysis shows that the use of this fiber allows extending the sensing range between 2.4 and 4 times the best previous results, which is a remarkable result in designing long-range multifunctional medical devices exploiting scattering-level multiplexing. In addition, since the fiber attenuation has a peak at 1535 nm, it is possible to optimize the working range of the OBR, simultaneously adjusting the spatial resolution and sensing length. Future work will revolve on exploring OBR-SLMux at wavelength over 1600 nm, and on the exploitation of the polarization-dependent properties of the fiber.

CRediT authorship contribution statement

Daniele Tosi: Conceptualization, Methodology, Investigation, Formal analysis, Data curation, Writing - original draft, Funding acquisition. **Carlo Molardi:** Conceptualization, Investigation, Writing - review & editing, Funding acquisition. **Wilfried Blanc:** Conceptualization, Resources, Writing - review & editing, Funding acquisition.

Declaration of Competing Interest

The authors declare that they have no known competing financial interests or personal relationships that could have appeared to influence the work reported in this paper.

Acknowledgments

The research was funded by Nazarbayev University, under grants SMARTER (code: 091019CRP2117), EPICGuide (code: 240919FD3908), and FOSTHER (code: 090118FD5314). This work was partly supported by ANR Projects Nice-DREAM (ANR-14-CE07-0016-03) and NanoSlim (ANR-17-CE08-0002).

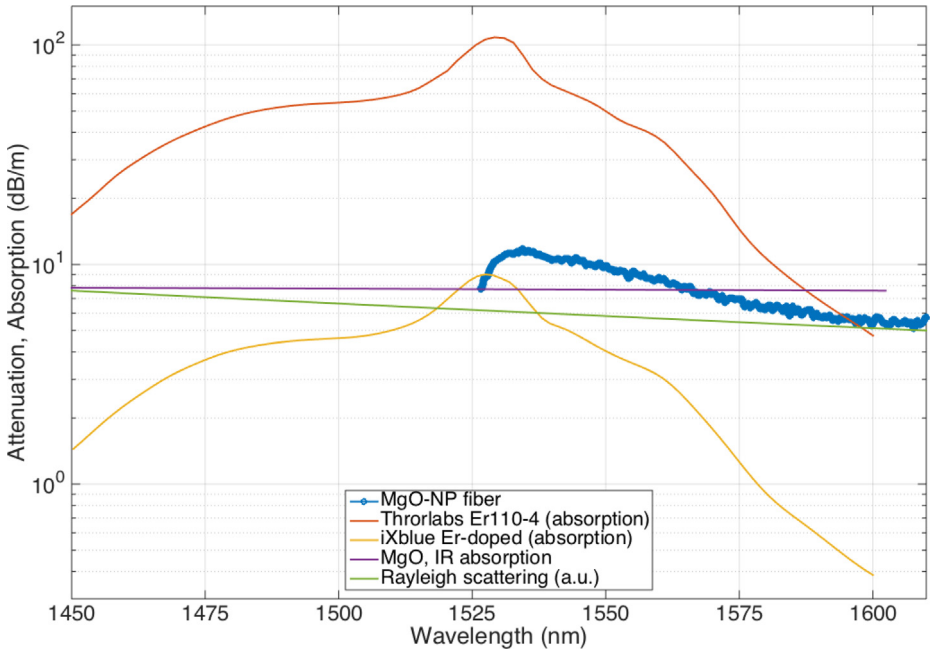

Fig. 10. Comparison of the MgO-NP attenuation spectrum, measured on the OBR, with other type of fiber losses: Thorlabs Er110-4 fiber, heavily Er-doped (absorption spectrum); iXblue Er-doped fiber, light doping (absorption spectrum); absorption spectrum of MgO, reported at infrared wavelength (absorption spectrum, normalized) [29]; Rayleigh scattering theoretical pattern, normalized to match the MgO-NP losses [16].

References

[1] X. Bao, L. Chen, Recent progress in distributed fiber optic sensor, Sensors 12 (7) (2012) 8601–8639.
[2] E.G. Macchi, et al., Optical fiber sensors-based temperature distribution measurement in ex vivo radiofrequency ablation with submillimeter resolution, J. Biomed. Opt. 19 (11) (2014) 117004.
[3] A. Yan, et al., Distributed optical fiber sensors with Ultrafast laser enhanced rayleigh backscattering profiles for real-time monitoring of solid oxide fuel cell operations, Sci. Rep. 7 (1) (2017) 9360.
[4] M. Froggatt, J. Moore, High-spatial-resolution distributed strain measurement in optical fiber with Rayleigh scatter, Appl. Opt. 37 (10) (1998) 1735.
[5] F. Parent, et al., Intra-Arterial Image Guidance With Optical Frequency Domain Reflectometry Shape Sensing, IEEE Trans. Medical Imaging 38 (2) (2018) 482–492.
[6] F. Parent, et al., Enhancement of accuracy in shape sensing of surgical needles using optical frequency domain reflectometry in optical fibers, Biomed. Opt. Express 8 (4) (2017) 2210–2221.
[7] T. Ayupova, et al., Fiber Optic Reflector-Less Refractive Index Distributed Multi-Sensors by Scattering-Level Multiplexing with MgO Nanoparticle-Doped Fibers, IEEE Sens. J. 20 (5) (2020) 2504–2510.
[8] M. Sypabekova, et al., Fiber optic refractive index sensors through spectral detection of Rayleigh backscattering in a chemically etched MgO-based nanoparticle-doped fiber, Opt. Lett. 43 (24) (2018) 5945–5948.
[9] P.J. Thomas, J.O. Hellevang, A high response polyimide fiber optic sensor for distributed humidity measurements, Sens. Actuat. B: Chem. 270 (2018) 417–423.
[10] A. Kiourti, K.S. Nikita, A review of implantable patch antennas for biomedical telemetry: Challenges and solutions, IEEE Antennas and Propagation Mag. 54 (3) (2012) 210–228.
[11] P.S. Westbrook, et al., Continuous multicore optical fiber grating arrays for distributed sensing applications, J. Lightwave Technol. 35 (6) (2017) 1248–1252.
[12] J. Clement, G. Torregrosa, J. Hervás, D. Barrera, S. Sales, C.R. Fernández-Pousa, Interrogation of a sensor array of identical weak FBGs using dispersive incoherent OFDR, IEEE Photon. Technol. Lett. 28 (10) (2016) 1154–1156.
[13] F. Monet, S. Loranger, V. Lambin-Iezzi, A. Drouin, S. Kadoury, R. Kashyap, The ROGUE: a novel, noise-generated random grating, Opt. Expr. 27 (10) (2019) 13895–13909.
[14] M.A. Soto, et al., Distributed temperature sensor system based on Raman scattering using correlation-codes, Electron. Lett. 43 (16) (2007) 862–864.
[15] Z. Zhao, M.A. Soto, M. Tang, L. Thévenaz, Distributed shape sensing using Brillouin scattering in multi-core fibers, Opt. Expr. 24 (22) (2016) 25211–25223.
[16] G. Agrawal, Applications of nonlinear fiber optics, Elsevier, 2001.
[17] A. Beisenova, A. Issatayeva, S. Korganbayev, C. Molardi, W. Blanc, D. Tosi, Simultaneous Distributed Sensing on Multiple MgO-doped High Scattering Fibers by Means of Scattering-level Multiplexing, J. Lightwave Technol. 37 (13) (2019) 3413–3421.
[18] A. Beisenova, et al., Multi-fiber distributed thermal profiling of minimally invasive thermal ablation with scattering-level multiplexing in MgO-doped fibers, Biomed. Opt. Express 10 (3) (2019) 1282–1296.
[19] A. Beisenova, A. Issatayeva, I. Iordachita, W. Blanc, C. Molardi, D. Tosi, Distributed fiber optics 3D shape sensing by means of high scattering NP-doped fibers simultaneous spatial multiplexing, Opt. Expr. 27 (16) (2019) 22074–22087.
[20] P.S. Westbrook, et al., Kilometer length, low loss enhanced back scattering fiber for distributed sensing, IEEE 25th Optical Fiber Sensors Conference (OFS), 2017, pp. 1–5.
[21] S. Loranger, M. Gagné, V. Lambin-Iezzi, R. Kashyap, Rayleigh scatter based order of magnitude increase in distributed temperature and strain sensing by simple UV exposure of optical fibre, Sci. Rep. 5 (2015) 11177.
[22] W. Blanc, C. Guillermier, B. Dussardier, Composition of nanoparticles in optical fibers by secondary ion mass spectrometry, Opt. Mater. Express 2 (11) (2012) 1504–1510.
[23] W. Blanc, B. Dussardier, Formation and applications of nanoparticles in silica optical fibers, J. Opt. 45 (3) (2016) 247–254.
[24] M. Froggatt, Distributed measurement of the complex modulation of a photo-induced Bragg grating in an optical fiber, Appl. Opt. 35 (25) (1996) 5162–5164.
[25] C. Molardi, T. Paixao, A. Beisenova, R. Min, P. Antunes, C. Marques, W. Blanc, D. Tosi, Fiber Bragg Grating (FBG) Sensors in a High-Scattering Optical Fiber Doped with MgO Nanoparticles for Polarization-Dependent Temperature Sensing, Appl. Sci. 9 (15) (2019) 3107.
[26] S. Korganbayev, et al., Refractive index sensor by interrogation of etched MgO nanoparticle-doped optical fiber signature, Photon. Technol. Lett. 31 (15) (2019) 1253–1256.
[27] J.W. Arkwright, et al., Design of a high-sensor count fibre optic manometry catheter for in-vivo colonic diagnostics, Opt. Express 17 (25) (2009) 22423.
[28] J.W. Arkwright, et al., In-vivo demonstration of a high resolution optical fiber manometry catheter for diagnosis of gastrointestinal motility disorders, Opt. Express 17 (6) (2009) 4500.
[29] D. Tosi, et al., Performance analysis of scattering-level multiplexing (SLMux) in distributed fiber-optic backscatter reflectometry physical sensors, Sensors 20 (2595) (2020).
[30] A.M. Hofmeister, E. Keppel, A.K. Speck, Absorption and reflection infrared spectra of MgO and other diatomic compounds, Monthly Notices of the Royal Astronomical Soc. 345 (1) (2003) 16–38.